Future Changes to El Niño Teleconnections over the North Pacific and North America

JONATHAN D. BEVERLEY,[a] MATTHEW COLLINS,[a] F. HUGO LAMBERT,[a] AND ROBIN CHADWICK[b,c]

[a] *College of Engineering, Mathematics and Physical Sciences, University of Exeter, Exeter, United Kingdom*
[b] *Met Office Hadley Centre, University of Exeter, Exeter, United Kingdom*
[c] *Global Systems Institute, University of Exeter, Exeter, United Kingdom*

(Manuscript received 16 November 2020, in final form 28 April 2021)

ABSTRACT: El Niño–Southern Oscillation (ENSO) is the leading mode of interannual climate variability, and it exerts a strong influence on many remote regions of the world, for example in northern North America. Here, we examine future changes to the positive-phase ENSO teleconnection to the North Pacific/North America sector and investigate the mechanisms involved. We find that the positive temperature anomalies over Alaska and northern North America that are associated with an El Niño event in the present day are much weaker, or of the opposite sign, in the CMIP6 abrupt $4\times CO_2$ experiments for almost all models (22 out of 26, of which 15 have statistically significant differences). This is largely related to changes to the anomalous circulation over the North Pacific, rather than differences in the equator-to-pole temperature gradient. Using a barotropic model, run with different background circulation basic states and Rossby wave source forcing patterns from the individual CMIP6 models, we find that changes to the forcing from the equatorial central Pacific precipitation anomalies are more important than changes in the global basic state background circulation. By further decomposing this forcing change into changes associated with the longitude and magnitude of ENSO precipitation anomalies, we demonstrate that the projected overall eastward shift of ENSO precipitation is the main driver of the temperature teleconnection change, rather than the increase in magnitude of El Niño precipitation anomalies, which is nevertheless seen in the majority of models.

KEYWORDS: El Niño; Teleconnections; Climate change

1. Introduction

El Niño–Southern Oscillation (ENSO) is the leading mode of interannual climate variability, and it modulates the climate in many regions of the world (e.g., Horel and Wallace 1981; Ropelewski and Halpert 1986). Among the most prominent of the teleconnections associated with ENSO is its influence on the winter climate of North America. In the present day, an El Niño event usually leads to an anomalously deep Aleutian low, as a result of the propagation of Rossby waves forced by precipitation in the central Pacific. This anomalous cyclonic circulation, centered over the North Pacific, drives the advection of warmer air across much of northern North America and Alaska. Given its importance to the climate of North America, it is therefore important to understand how this teleconnection may change under global warming.

The two main factors that will determine future changes to ENSO teleconnections are changes in the time mean background state and changes to ENSO properties, such as the magnitude and spatial pattern of El Niño events (Meehl et al. 2006; Yeh et al. 2018). Projections of future changes to the amplitude of El Niño events are uncertain and tend to be model dependent, with some models showing an increase in intensity, some showing a decrease, and some with little change (e.g., van Oldenborgh et al. 2005; Collins et al. 2010; Guilyardi et al. 2012) and any changes are often not significantly different from long-term variability (Stevenson 2012).

However, there is a greater amount of intermodel agreement that precipitation anomalies associated with El Niño will move eastward under global warming. This is largely related to a weakening of the Walker circulation and enhanced equatorial SST warming, particularly in the east Pacific, which reduces the east–west temperature gradient and reduces the barrier to convection there (Knutson and Manabe 1995; Meehl and Washington 1996; Boer et al. 2004; Xie et al. 2010; Power et al. 2013). There is "medium confidence" (IPCC AR5; Christensen et al. 2013) that such a shift of convection and associated upper-level divergence will result in an overall eastward shift of ENSO teleconnection patterns, although the exact nature of changes in the North Pacific/North America sector varies across different studies (Meehl et al. 2006; Meehl and Teng 2007; Sterl et al. 2007; Müller and Roeckner 2008; Kug et al. 2010; Brown et al. 2020). It also remains unclear how much of this shift is attributable to changes in the extratropical mean basic state due to background warming and how much relates to the eastward shift of the El Niño Rossby wave source regions in the equatorial Pacific. Some studies suggest that changes to the mean state in the extratropics make an important contribution (Müller and Roeckner 2008). Meehl and Teng (2007) found that a reduction in streamfunction occurs independent of ENSO near the west coast of North America in association with increased greenhouse gas concentrations, which they argue contributes to the eastward shift of the teleconnection pattern. However, other studies, such as Kug et al. (2010), have found that changes in the equatorial Pacific are most important. The majority of studies described above have used either single models or small multimodel ensembles, which is likely to explain the varying responses seen, due to differences in El Niño simulation and impacts of projected warming across models, among other reasons. By using a large ensemble of CMIP6 models in this study, we aim to overcome some of this uncertainty by reducing model dependence.

Corresponding author: Jonathan D. Beverley, j.d.beverley@exeter.ac.uk

DOI: 10.1175/JCLI-D-20-0877.1

A simple linear barotropic model can be a useful tool to help understand the propagation of Rossby waves on different basic states and with different dynamical forcings. Such a model has been previously used to explore tropical–extratropical interactions (e.g., Ambrizzi et al. 1995; O'Reilly et al. 2018), including those associated with ENSO. For example, Hoerling et al. (1997) showed that the nonlinear relationship between SST and rainfall in the equatorial Pacific alone may be responsible for the nonlinearity of the extratropical teleconnection response between El Niño and La Niña years.

The idealized nature of the barotropic model used here, which is run by applying a Rossby wave source forcing to a specified basic state, means that the contribution of changes to the forcing and changes to the basic state in driving changes to extratropical teleconnections can be determined. By using basic states and forcings from individual CMIP6 models, we are also able to determine any uncertainty in the relative role of these changes across the ensemble.

The rest of the paper is arranged as follows. The data and models are outlined in section 2, including details of the simulations used and an overview of the barotropic model. Analysis of CMIP6 data and the barotropic model experiments are presented in section 3. We conclude in section 4.

2. Data and methods

a. Models and simulations

In this study we utilize two experiments from phase 6 of the Coupled Model Intercomparison Project (CMIP6; Eyring et al. 2016), both of which form part of the "DECK" core simulations. The baseline simulations against which the climate change experiments are compared are the preindustrial control (piControl). These have the advantage of being long simulations (we use 430 years for each model), and they are run with forcings set to represent conditions in 1850 and are all in quasi-stable equilibrium.

The climate change experiment used, abrupt-4×CO_2, involves an abrupt quadrupling of CO_2 concentrations from the global annual mean 1850 value used in the piControl simulations. Although very idealized, these experiments provide a clearer signal of the impact of changing CO_2 forcing, and enable us to examine the physical processes involved. For the majority of models, these experiments are 150 years in length. To account for the fact that equilibrium will not have been reached by the end of the simulation, and to maximize the number of years available for analysis, we performed Fourier harmonic analysis on the data to remove the long-term trend and variations with a period of longer than 10 years. This filtering introduces abnormalities at the beginning and end of the time series, so we remove these years before analysis. A list of the models used, along with the total number of years, can be found in Table 1.

b. Indices and analysis

The variables used for the analysis in this paper are December–February (DJF) mean surface temperature, 200- and 850-hPa wind, mean sea level pressure, and precipitation rate. In this study, El Niño anomalies shown are relative to neutral years. El Niño and neutral years are defined using SST anomalies in the Niño-3.4 region (5°N–5°S, 170°–120°W; Trenberth 1997). The Niño-3.4 index time series from each model and for both piControl and abrupt-4×CO_2 [N3.4(t)] was used to identify years as El Niño or neutral based on the standard deviation of the piControl Niño-3.4 index, namely N3.4 $> 1.0\sigma_p$ or $-1.0\sigma_p \leq$ N3.4 $\leq 1.0\sigma_p$ for El Niño or neutral years respectively, where σ_p is the standard deviation of each model's piControl Niño-3.4 index time series.

c. Linear barotropic model

In section 3b we use a linear barotropic model for a single level in the atmosphere to help understand and separate the contribution of changes to the basic state and forcing to the changes in the North America teleconnection. This model is based on the damped barotropic vorticity equation, following Hoskins and Ambrizzi (1993):

$$\left(\frac{\partial}{\partial t} + u_\psi \cdot \nabla\right)\zeta = F - \lambda\xi - \mu\nabla^4\xi, \tag{1}$$

where u_ψ is the rotational wind field, ζ is the absolute vorticity, ξ is the relative vorticity, $F = \overline{F} + F'$ is a constant forcing, λ is a linear damping with a time scale of 10 days, and $\mu = 2.4 \times 10^{16}\,\mathrm{m^4\,s^{-1}}$ is a diffusion coefficient. Note that $\overline{F}$ is chosen to keep the model stationary in the absence of any additional forcing so that it exactly maintains the basic state:

$$\overline{F} = u_\psi \cdot \nabla\zeta + \lambda\xi + \mu\nabla^4\xi. \tag{2}$$

The anomalous forcing (F') is chosen to be the Rossby wave source calculated using anomalous divergence associated with El Niño. Following Sardeshmukh and Hoskins (1988), this is given by

$$F' = -\overline{\zeta}D' - \mathbf{v}'_\chi \cdot \nabla\overline{\zeta}, \tag{3}$$

where $\mathbf{v}_\chi$ is the divergent wind field and D is the divergence. Here, overbars and primes represent climatological and anomaly fields, respectively. In this study, only the anomalous divergence that is directly associated with El Niño precipitation in the equatorial Pacific between around 15°N–15°S is retained. Therefore, to the north and south of this band the $-\overline{\zeta}D'$ term goes to zero and the forcing becomes $-\mathbf{v}'_\chi \cdot \nabla\overline{\zeta}$. This transition is smoothed around 5° either side of the 15°N/15°S boundary, and this blended forcing field is applied in several tropical Pacific regions, details of which can be found in section 3b.

The basic state used is 200-hPa relative vorticity from the individual CMIP6 piControl and abrupt-4×CO_2 simulations. By using input fields from 26 CMIP6 models, this effectively gives us an ensemble of barotropic model experiments. While the choice of the 200-hPa level can be a source of uncertainty in barotropic model experiments, we found that our results were similar when using the 150- and 250-hPa levels. An upper tropospheric level is used as this where the forcing from outflow (divergence) associated with tropical precipitation tends to peak and is also the level at which strong vorticity gradients are present, which act as waveguides for Rossby waves.

TABLE 1. List of CMIP6 models included in the study, the number of years used from each experiment, the standard deviation of the Niño-3.4 index time series for piControl (N3.4σ_p) and abrupt-4×CO_2 (N3.4σ_a), the number of El Niño events in each model simulation, the p value for the NNAM temperature anomaly change (bold for models that are significant at the 5% level), and the amplitude and longitude changes of El Niño precipitation anomalies, defined using the method described in section 3.

Model	No. of piControl years	N3.4σ_p	No. of El Niño years	No. of abrupt-4×CO_2 years	N3.4σ_a	No. of El Niño years	Temperature anomaly change p value	Amplitude change	Longitude change
ACCESS-CM2	430	1.02	76	110	0.91	12	0.14	1.70	3.8
AWI-CM-1-1-MR	430	0.91	49	110	1.22	24	**<0.001**	1.24	13.1
BCC-CSM2-MR	430	1.13	64	110	0.75	8	0.89	1.24	25.9
BCC-ESM1	430	0.75	75	110	0.53	8	**0.002**	1.88	22.5
CanESM5	430	0.63	60	110	0.71	23	0.65	1.32	25.3
CESM2-WACCM	430	1.21	67	110	1.03	8	0.08	1.29	18.8
CIESM	430	1.01	66	110	0.66	8	**0.02**	0.84	10.0
CMCC-CM2-SR5	430	1.10	61	110	1.75	30	**0.02**	1.30	43.8
CNRM-CM6-1	430	0.98	76	110	1.15	25	**0.002**	1.19	21.1
CNRM-ESM2-1	430	1.09	66	110	1.25	29	0.06	1.18	21.1
E3SM-1-0	430	1.05	62	110	1.52	34	**<0.001**	1.06	37.0
EC-Earth3-Veg	430	0.91	69	110	1.43	35	0.08	1.16	36.6
FGOALS-f3-L	430	1.44	83	110	1.48	22	**0.03**	1.05	34.0
GISS-E2-1-H	430	0.97	72	110	1.61	39	**0.02**	1.38	50.0
HadGEM3-GC31-LL	430	0.96	68	110	0.87	16	0.21	1.22	16.9
INM-CM5-0	430	0.46	78	110	0.49	19	0.82	1.62	0.0
IPSL-CM6A-LR	430	1.01	71	700	1.27	173	**<0.001**	2.20	5.0
MCM-UA-1-0	430	0.63	57	400	0.77	83	**<0.001**	1.48	18.8
MIROC6	430	0.91	58	210	1.49	57	**<0.001**	1.23	30.0
MIROC-ES2L	430	1.27	73	110	1.62	31	0.12	1.13	30.9
MPI-ESM1-2-HR	430	0.84	70	110	0.91	20	**0.003**	0.88	30.9
MRI-ESM2-0	430	1.04	65	110	1.22	27	**<0.001**	1.24	34.9
NorCPM1	430	1.01	68	110	0.55	5	0.22	0.81	−10.0
SAM0-UNICON	430	1.14	70	110	1.67	35	**<0.001**	1.15	43.8
TaiESM1	430	1.30	78	110	1.23	18	**0.001**	0.76	38.8
UKESM1-0-LL	430	1.06	73	110	0.82	12	**<0.001**	2.21	13.1

Equation (1) is solved using spectral harmonics with triangular truncation at wavenumber 85 (T85). The constant forcing F' is applied to the basic state and the model is integrated forwards for 30 days. The response reaches equilibrium shortly after 14 days into the simulation, so the results we present here are for the average over days 20–25.

3. Results

a. Present-day teleconnection and projected changes

The ability of the CMIP6 models, listed in Table 1, to simulate the present-day El Niño teleconnection to the North Pacific and North America is first evaluated in Fig. 1, which shows the 850-hPa wind and surface temperature anomalies in El Niño years for both ERA5 reanalysis (Hersbach et al. 2020) and the CMIP6 multimodel mean (MMM). In the present day reanalysis (1979–2018) an El Niño event causes circulation anomalies similar to those associated with the positive phase of the Pacific–North American pattern (PNA; Wallace and Gutzler 1981), with an anomalously deep Aleutian low that leads to the advection of warmer air northward, resulting in positive temperature anomalies across large parts of northern North America (Fig. 1a).

Overall, the anomaly patterns for the CMIP6 MMM are qualitatively similar to the reanalysis, with cyclonic wind anomalies centered over the North Pacific associated with an anomalously deep Aleutian low and positive temperature anomalies over much of northern North America. The main differences between ERA5 and the CMIP6 MMM are in the magnitude of both the wind and temperature anomalies, with generally weaker magnitudes for both in CMIP6, although this is largely an artifact of averaging across the ensemble. The anticyclonic anomaly centered over eastern North America is also fairly poorly represented by the CMIP6 models, with much weaker winds than in the reanalysis. All models have an anomalous cyclonic circulation over the North Pacific, and Fig. 1c shows the temperature anomaly in the CMIP6 models averaged over 50°–70°N, 160°–100°W (the red box in Fig. 1b, hereafter NNAM), as well as the equivalent values for the MMM and ERA5. Although there is some diversity among the models in the location, spatial extent, and magnitude of the positive temperature anomalies, all have an overall positive anomaly when averaging over this region and a large number have a similar magnitude to ERA5. It has previously been shown that internal variability and sampling differences (i.e.,

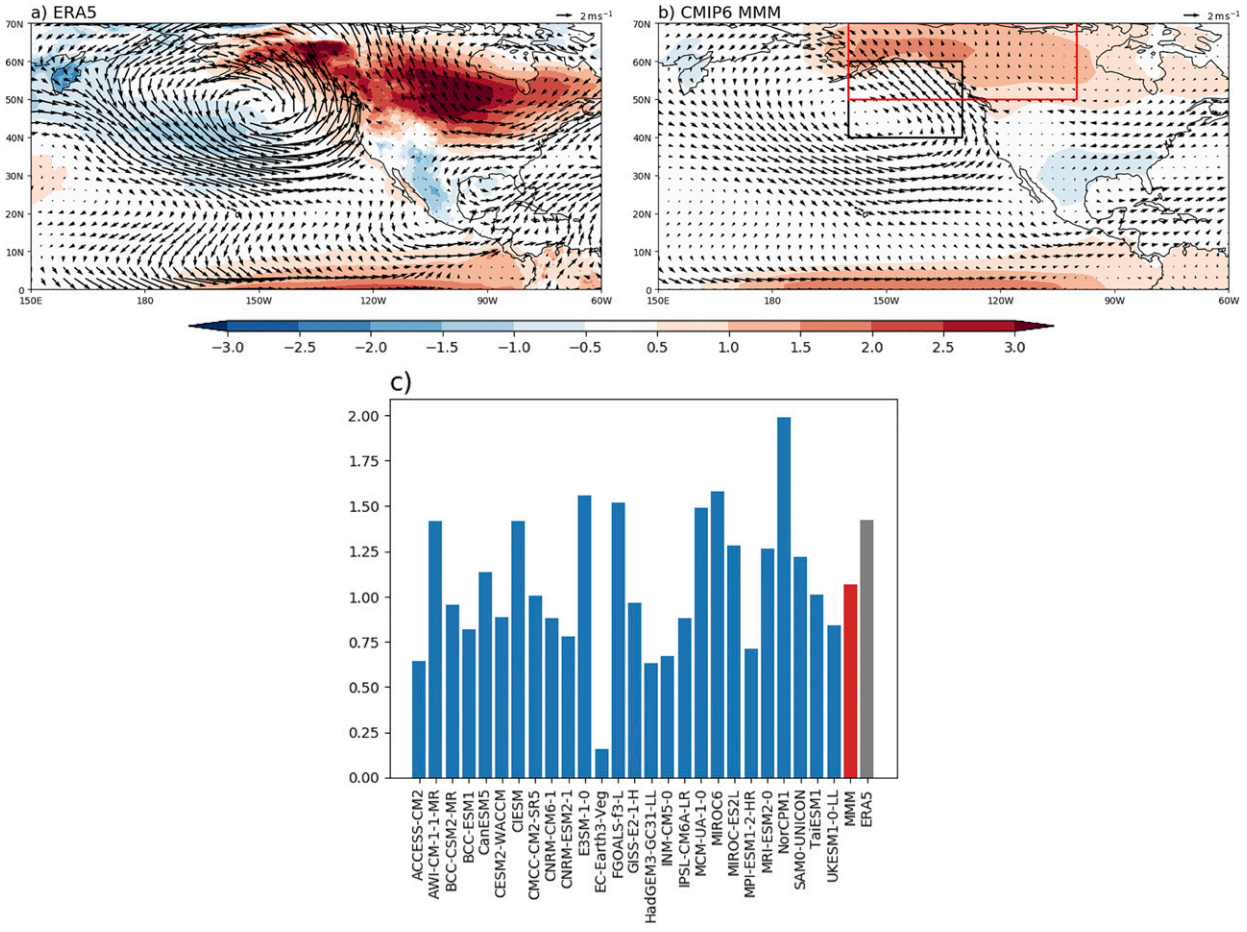

FIG. 1. (a) ERA5 and (b) CMIP6 multimodel mean DJF temperature anomaly (2-m temperature for ERA5 and surface temperature for CMIP6) and 850-hPa wind anomaly (vectors) in composite El Niño years. (c) Surface temperature anomalies averaged over 50°–70°N, 160°–100°W [the NNAM region, red box in (b)], for composite El Niño events in each individual CMIP6 model (blue bars), the MMM (red bar), and ERA5 (gray bar). In the present day (ERA5) El Niño events are associated with an anomalous cyclonic circulation centered over the North Pacific and positive temperature anomalies over much of northern North America. This pattern is fairly well captured by the CMIP6 models; most have a North America temperature anomaly with a magnitude that is comparable to ERA5. The boxes in (b) are used in the subsequent analysis.

variations in the number of El Niño events in different models) can have a significant impact on the magnitude of surface temperature anomalies over North America (Deser et al. 2018). However, this does not appear to be an issue here, with relatively small differences in the number of El Niño events across the CMIP6 piControl simulations, and no clear relationship between the number of events and the magnitude of temperature anomalies (Table 1).

The MMM change in El Niño–related surface temperature anomalies in the abrupt-4×CO_2 simulations compared to piControl is shown in Fig. 2a. It is immediately noticeable that the positive temperature anomalies that are present in the piControl MMM (Fig. 1b) are much reduced in the abrupt-4×CO_2 simulations. This is somewhat different from the findings of Brown et al. (2020), who found that the temperature teleconnection, while weaker over Alaska, is amplified over Canada. However, several aspects of their study differ from ours. First, they use a different subset of models, with a mix of both CMIP5 and CMIP6 experiments, and there is only an overlap of five models with our study. Only two of the models that we analyzed have a pattern of temperature anomaly change that is similar to that of Brown et al. (2020), and neither of these were used in their study. This suggests that differences in analysis technique are likely to be largely responsible. For example, Brown et al. (2020) use the entire length of the abrupt-4×CO_2 time series, whereas we exclude the first 20 years to lessen the influence of the nonlinear trends early in the simulations. There are also likely to be differences with the detrending used, as well as the definition of El Niño years. We tested the sensitivity of our results to the detrending technique, as well as the method for defining El Niño years, and found them to be very similar in both cases (not shown), which suggests that they are robust.

Figure 2b shows the temperature changes averaged over the NNAM region and while there is a reasonable level of

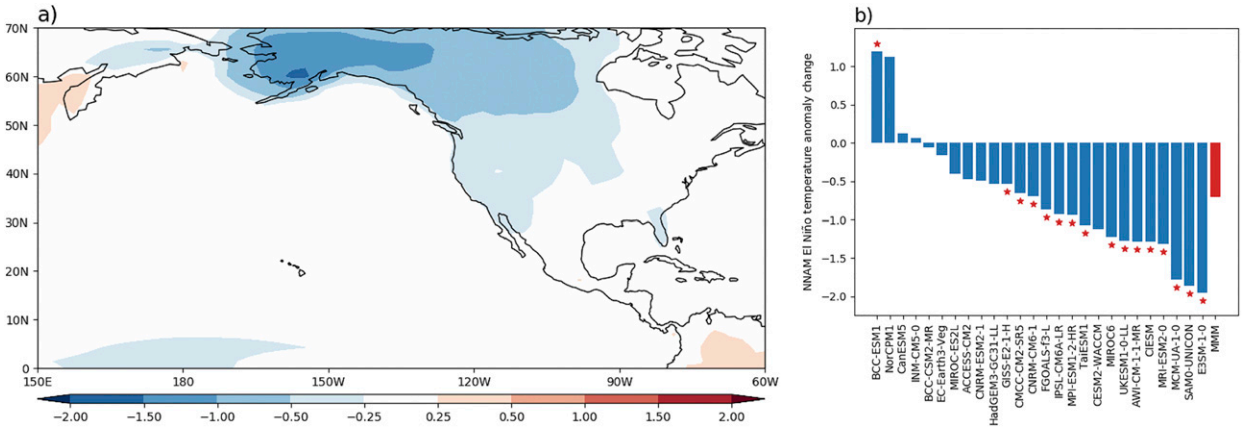

FIG. 2. (a) Multimodel mean abrupt-4×CO_2 minus piControl surface temperature anomaly in El Niño years. (b) Change in surface temperature anomaly averaged over the northern North America (NNAM) region (shown as the red box on Fig. 1b), for each CMIP6 model (blue bars) and the MMM (red bar). In the abrupt-4×CO_2 simulations the positive El Niño temperature anomalies are weaker in almost all models across much of northern North America. The models in (b) are arranged from positive to negative temperature anomaly change, and this order is retained in subsequent figures. Red stars indicate models with a temperature anomaly change that is significant at the 5% level, and the *p* values for all models are listed in Table 1.

variability from model to model, 22 out of the 26 models agree on the sign of this change, with only four models showing a positive change, and the change in 16 models is significant at the 5% level, as indicated by the red stars (including one that simulates a positive change). Indeed, in nine models, the El Niño temperature anomalies when averaged over northern North America switch from positive in piControl to negative in abrupt-4×CO_2. This consistent response is found both in models that have an increase and a decrease in the standard deviation of the Niño-3.4 index time series between piControl and abrupt-4×CO_2 (Table 1).

b. *Investigating the cause of changes to the North American teleconnection*

We now investigate the possible causes of these changes to the North American teleconnection. As described in the introduction, previous studies have shown that precipitation associated with El Niño is projected to shift eastward under global warming. Recent studies have shown that the frequency and intensity of eastern Pacific El Niño events are projected to increase in warming simulations, which is linked to the weakening of the east–west temperature gradient in the equatorial Pacific (Cai et al. 2014, 2018; Fredriksen et al. 2020). This weakening of the temperature gradient is also found in the models analyzed here, as well as both a strengthening and an eastward shift of the multimodel mean El Niño precipitation anomalies between piControl and abrupt-4×CO_2 (Fig. 3). However, we do not analyze changes to ENSO diversity and frequency of different El Niño types in this study. As a source of Rossby waves, these changes to the precipitation would be expected to result in an eastward shift of the anomalous circulation over the North Pacific, as shown in previous studies (Christensen et al. 2013). We therefore next examine the relationship between the changes to the circulation (winds) over the North Pacific and the temperature anomalies over North America.

Figure 4 shows the change in the 850- and 200-hPa meridional winds for abrupt-4×CO_2 minus piControl, averaged over a North Pacific box (40°–60°N, 160°–130°W, plotted as a black box on Fig. 1b, hereafter NPAC) against NNAM temperature anomaly change. The NPAC region was chosen as the meridional wind in that region is strongly correlated with the temperature anomaly over North America in both the reanalysis and piControl runs (not shown). At both upper and lower levels, the change in the strength of meridional wind anomalies in NPAC is closely related to the change in the NNAM surface temperature anomaly across the CMIP6 models, with correlations of 0.88 and 0.87 for 850 and 200 hPa, respectively. This strong relationship also suggests that the changes to the North American temperature teleconnection that are seen in Fig. 2 are dominated by changes to the circulation anomalies, rather than changes to the equator-to-pole temperature gradient, whereby higher latitudes are projected to warm faster than lower latitudes (Holland and Bitz 2003).

It is also noticeable that the majority of models (24 out of 26) have a negative change in the magnitude of both 850- and 200-hPa meridional wind anomalies (i.e., the southerly component of the wind in the region is weaker). This change could be due to either a shift in the location of the circulation anomalies or a weakening of the anomalous Aleutian low (or a combination of the two). Previous studies have shown that El Niño teleconnections are projected to shift eastward under global warming (Meehl and Teng 2007; Stevenson et al. 2012), and the IPCC AR5 report gave medium confidence of such a change.

We now investigate the relative contributions of changes to the magnitude of the North Pacific anomalous low pressure and shifts in its longitude to the change in NNAM temperature anomaly. Figure 5a shows the change in magnitude of the mean sea level pressure (MSLP) minima over the North Pacific (a positive value indicating a less deep anomalous low) against the NNAM temperature anomaly change. Potential shifts in

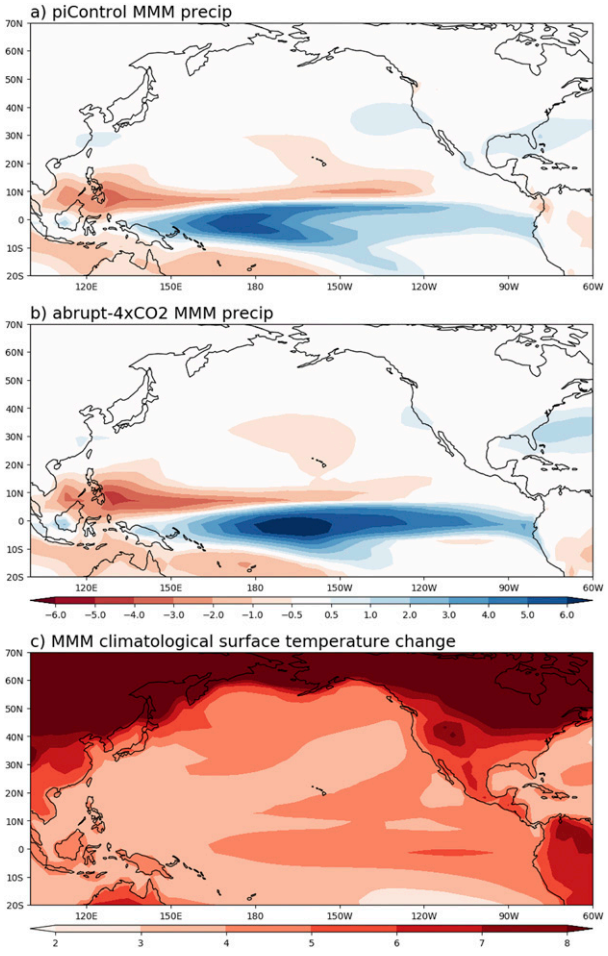

FIG. 3. (a) piControl and (b) abrupt-4×CO_2 multimodel mean precipitation anomaly in El Niño years. (c) Multimodel mean abrupt-4×CO_2 minus piControl climatological surface temperature. Precipitation associated with El Niño is projected to shift eastward and strengthen in the warming simulations, associated with greater surface temperature warming in the eastern equatorial Pacific.

the location of the MSLP minima are taken into account by finding the minimum value within a large North Pacific region separately for piControl and abrupt-4×CO_2, and then calculating the difference between the two. Similar to the meridional wind changes, the majority of CMIP6 models have an anomalous low that is weaker in abrupt-4×CO_2 than in piControl (18 out of 26 models). There is also a correlation of −0.62, significant at the 1% level, which suggests that changes to the magnitude of the MSLP minima play an important role in the changes to the NNAM temperature anomaly.

An eastward shift of the North Pacific anomalous cyclonic circulation would mean that air that is advected northward would originate from over the North American landmass, rather than the North Pacific. In DJF the air over this landmass is cooler than that over the Pacific Ocean at the same latitude, so the air advected over northern North America would be less anomalously warm than in the present day. In the CMIP6 models, the relationship between the change in the longitude of the MSLP minima and NNAM temperature anomaly change (Fig. 5b) is slightly weaker than for the magnitude change, although the correlation of −0.42 is still significant at the 5% level. This suggests that longitudinal changes in the location of the MSLP minima may also contribute to the NNAM temperature anomaly change.

Previous studies have shown that sampling and internal variability can result in diversity in El Niño composite fields and climate trends over North America (e.g., Deser et al. 2018; McKinnon and Deser 2018). However, in this study, there is no systematic difference in the number of El Niño events in models with significant versus nonsignificant temperature anomaly changes (Table 1), which suggests that sampling does not play a role here. Michel et al. (2020) estimated that 50–75 ENSO events are required to detect robust changes in the strength or position of the North Pacific anomalous low pressure, although this was under a low global warming scenario (+2°C warming) whereas the forcing in the abrupt-4×CO_2 simulations is much larger and so fewer events are required.

Having shown that there is a relationship between circulation changes and changes in the NNAM El Niño temperature anomaly, we next use a barotropic model to investigate the relative influence of changes to the Rossby wave forcing and changes to the basic state to the overall teleconnection changes. Analysis of these experiments can be found in the next section.

BAROTROPIC MODEL

We first determine the ability of the barotropic model (described in section 2c) to represent the present-day teleconnection by running an experiment using the basic state and forcing from the piControl multimodel mean. This forcing (F') is shown in Fig. 6a and was applied within the tropical Pacific region shown (30°N–30°S, 100°E–120°W). The other two forcing regions in Fig. 6a are used in subsequent experiments. The day 20–25 average wind anomalies from this experiment are shown in Fig. 6b, along with the equivalent MMM El Niño 200-hPa wind composite produced using piControl data (Fig. 6c). The barotropic model is able to simulate an anomalous cyclonic circulation over the North Pacific of realistic intensity, albeit with a center that is shifted southward compared to CMIP6 by around 5°–10°. This slight southward bias is likely to be due to the definition of the forcing region used, as there will also be contributions from midlatitude regions. However, as we are focusing on changes in the strength and longitudinal position of this circulation feature between piControl and abrupt-4×CO_2, the bias in the mean meridional position of the feature is not expected to impact our results. The response of the barotropic model in the equatorial Pacific region is not similar to the CMIP6 wind anomalies, but this is likely to be because the response here to forcing from tropical precipitation is baroclinic, and so not well represented by the barotropic model.

To further demonstrate the suitability of the barotropic model for use in understanding the teleconnection changes between piControl and abrupt-4×CO_2, we now compare for each CMIP6 model the wind anomaly changes between two

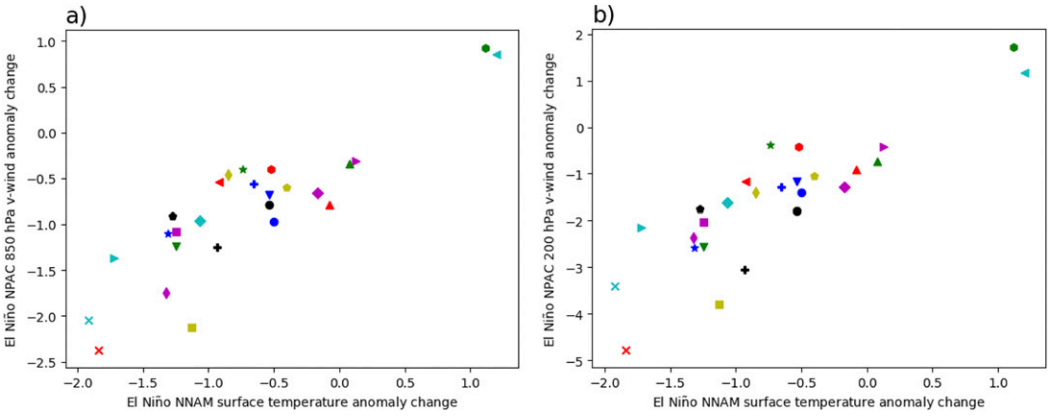

FIG. 4. (a) Change in El Niño surface temperature anomaly averaged over the NNAM region vs El Niño 850-hPa meridional wind anomaly averaged over the NPAC region (shown as a black box on Fig. 1b). (b) As in (a), but for the 200-hPa meridional wind anomaly. The symbols used for each CMIP6 model can be found in the appendix. The change in the North America El Niño temperature anomaly in the CMIP6 models is closely related to changes in the North Pacific meridional wind at both upper and lower levels, with correlations of 0.88 and 0.87 for 850 and 200 hPa, respectively, which are both statistically significant ($p < 0.001$). The p values for the surface temperature anomaly changes can be found in Table 1.

barotropic model experiments, one with piControl F' and basic state, and one with abrupt-4×CO_2 F' and basic state, to the wind anomaly changes from the full CMIP6 experiments. This is shown in Fig. 7 and the wind anomaly changes shown are for abrupt-4×CO_2 minus piControl meridional wind averaged over the same NPAC region used earlier. It can be seen that, despite its simplicity, the barotropic model is able to accurately capture the ensemble mean response, with a meridional wind change ($-1.57\,\mathrm{m\,s^{-1}}$) that is almost identical to that from the full CMIP6 simulations ($-1.56\,\mathrm{m\,s^{-1}}$), as well as a reasonable amount of the variability that exists within the CMIP6 ensemble, with a correlation of 0.57 between the anomaly changes from the barotropic model and those from the full CMIP6 simulations. In particular, the anomaly changes in some of the models that have the largest negative change, such as SAM0-UNICON and E3SM-1-0, are well represented by the barotropic model. There are some models that sit farther from the 1:1 line, particularly the two that have a positive NPAC wind change in the full CMIP6 simulations (BCC-ESM1 and NorCPM1), and there are a number of possible reasons for these differences, such as baroclinic or nonlinear processes or contributions from other forcing regions. However, the majority

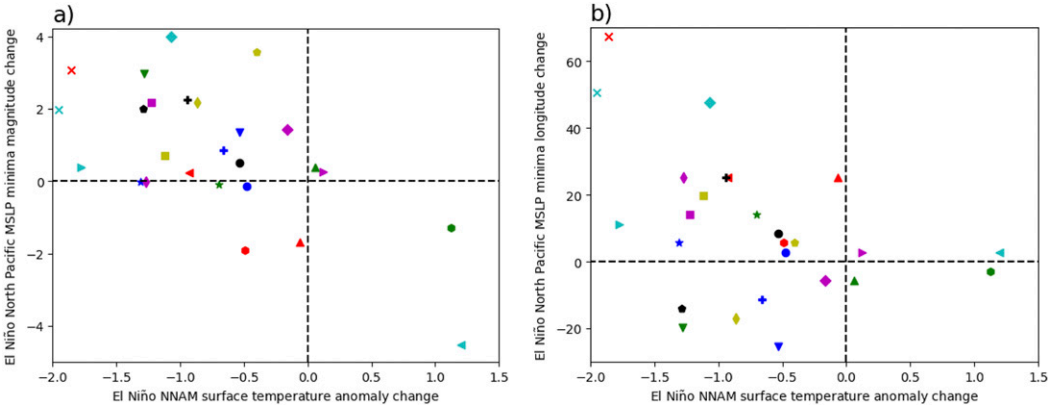

FIG. 5. (a) Change in the magnitude of MSLP minima in El Niño years in the North Pacific vs change in El Niño surface temperature anomaly averaged over the NNAM region. (b) As in (a), but for the change in longitude of the MSLP minima vs NNAM temperature anomaly. The horizontal and vertical dashed lines indicate zero change, and the symbols used for each CMIP6 model can be found in the appendix. The change in the North America El Niño temperature anomaly is related to both changes in the magnitude ($r = -0.62$, $p = 0.001$) and longitude ($r = -0.42$, $p = 0.03$) of the North Pacific anomalous low pressure. Together with the relationship in Fig. 4, this suggests that changes to the anomalous circulation are the main cause of changes to the North America El Niño temperature anomalies, rather than changes to the equator-to-pole temperature gradient. The p values for the surface temperature anomaly changes can be found in Table 1.

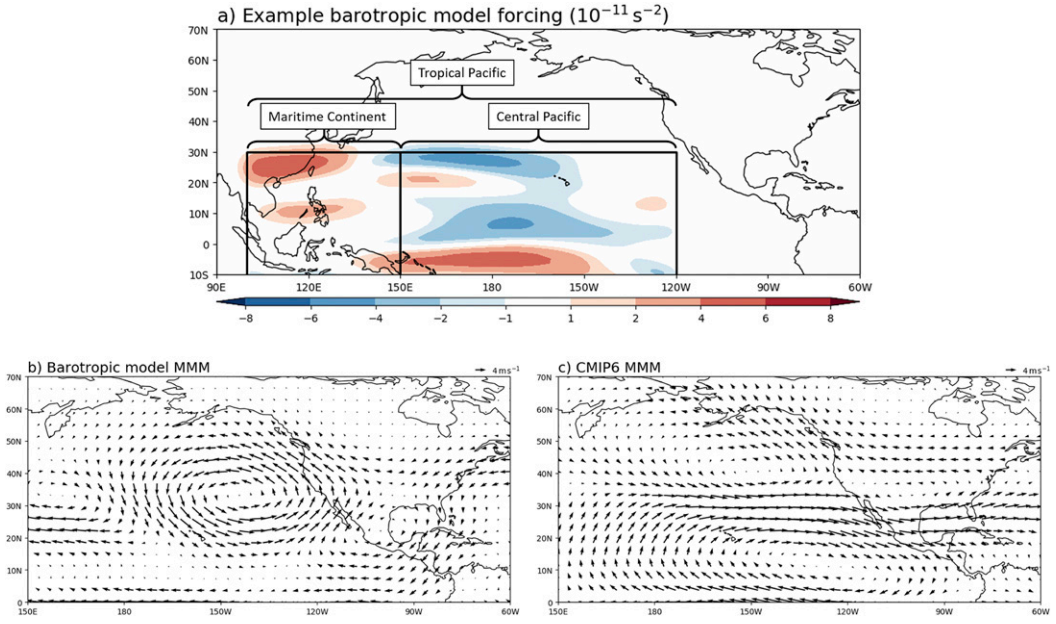

FIG. 6. (a) Example forcing field (F') used in the barotropic model experiments, and the different forcing regions used. (b) 200-hPa wind anomaly averaged over days 20–25 of the barotropic model experiment run using piControl MMM basic state and piControl anomalous El Niño forcing (F') shown in (a) [Eq. (3)]. (c) CMIP6 piControl MMM 200-hPa wind anomaly in El Niño years. The barotropic model is able to simulate an anomalous cyclone of realistic strength over the North Pacific, although it is centered slightly too far south compared to the CMIP6 MMM.

of models sit close to the 1:1 line and this, along with the close agreement in the ensemble mean response, suggests that the barotropic model can be used effectively to help further understand the causes of the teleconnection changes.

Also shown in Fig. 7 is the meridional wind change from these barotropic model experiments as a bar chart, for comparison with subsequent figures. The bars on these and all subsequent bar charts are arranged in the same order as in Fig. 2 (in order of their projected North America El Niño temperature anomaly change) and the red bar is the average. Models with the largest negative wind changes tend to be farther toward the right of the plot, although there is not as much of a ramp as in Fig. 2.

Previous studies have shown that forcing associated with the advection of the mean vorticity by the anomalous divergent wind [the second term on the right-hand side of Eq. (3)] in the subtropical Pacific is important in determining the extratropical

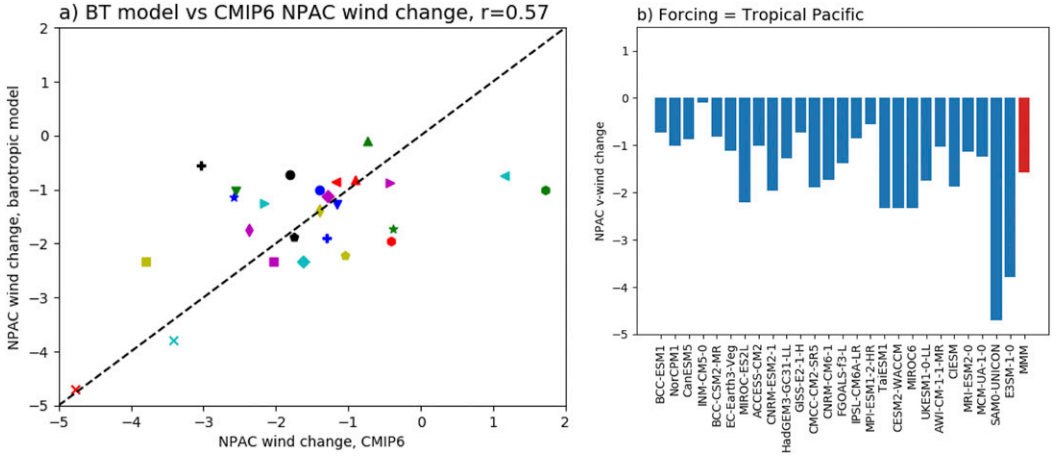

FIG. 7. (a) The 200-hPa meridional wind change averaged over the NPAC region from the barotropic model experiments varying both basic state and forcing vs the equivalent from the CMIP6 models. The dashed line is the 1:1 line, and the symbols used for each CMIP6 model can be found in the appendix. (b) The 200-hPa meridional wind change from the same barotropic model experiments, for comparison with Fig. 9. The barotropic model is able to accurately capture the ensemble mean response, as well as a reasonable amount of the intermodel variability.

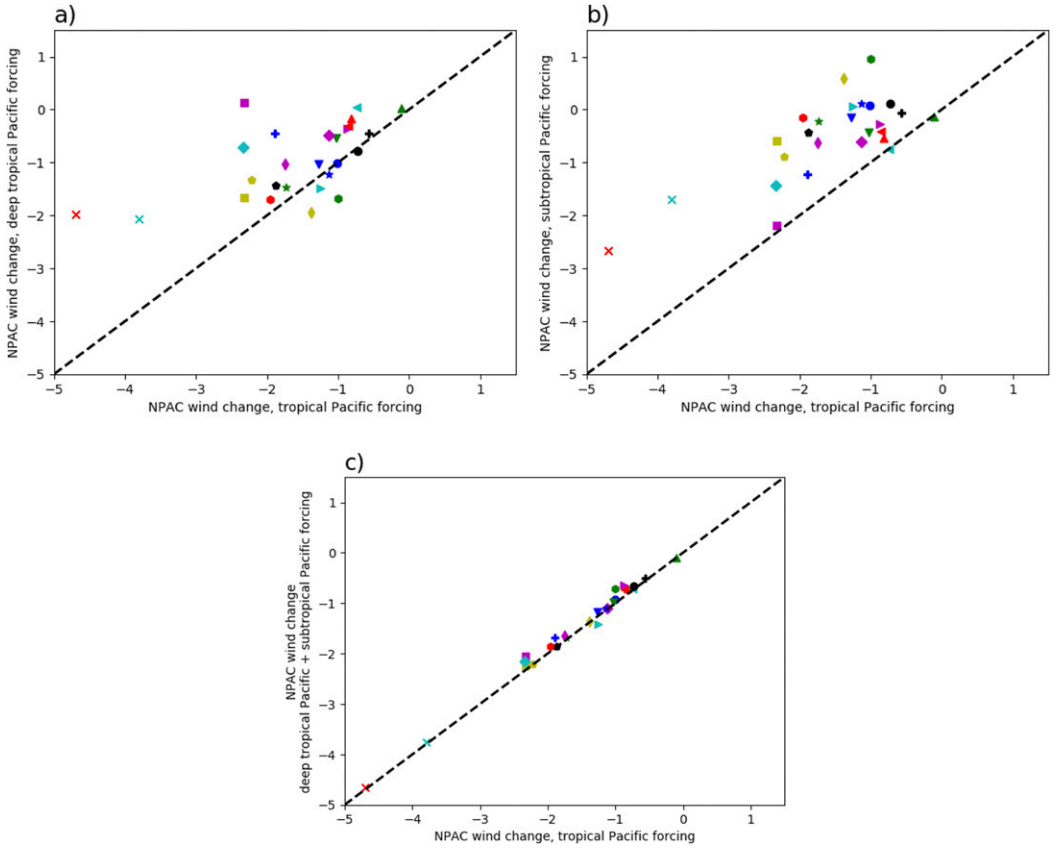

FIG. 8. The 200-hPa meridional wind change averaged over the NPAC region from barotropic model experiments varying both basic state and forcing when using different forcing regions. (a) Forcing in the deep tropical Pacific (20°N–20°S, 100°E–120°W) vs the full tropical Pacific. (b) Forcing in the subtropical Pacific (20°–30°N, 100°E–120°W) vs the full tropical Pacific. (c) Sum of the NPAC wind changes from the deep tropical Pacific and subtropical Pacific forcing experiments vs the full tropical Pacific forcing. The dashed line is the 1:1 line, and the symbols used for each CMIP6 model can be found in the appendix. For the majority of models, the NPAC wind changes in Fig. 7 are driven from the deep tropical Pacific, rather than the subtropical Pacific, although the latter does make a contribution in some models. The wind changes from the deep tropical Pacific and subtropical Pacific forcing experiments almost exactly add up to that from the full tropical Pacific forcing experiment, due to the linearity of the barotropic model.

response in barotropic model experiments (e.g., Grimm and Silva Dias 1995). To investigate its role in our experiments, we also performed experiments forcing only in the deep tropical Pacific (20°N–20°S, 100°E–120°W) and subtropical Pacific (20°–30°N, 100°E–120°W). The NPAC wind anomaly changes in these experiments compared to the change when using the full tropical Pacific forcing region are shown in Fig. 8. Due to the linearity of the barotropic model, the sum of the NPAC wind changes from the deep tropical and subtropical Pacific forcing experiments almost exactly equals the change in the full tropical Pacific forcing experiment (Fig. 8c), which allows us to determine the contribution from each of these forcing regions.

For the majority of models, the NPAC wind changes in Fig. 7 are largely driven from the deep tropical Pacific. This is illustrated in Fig. 8a, with most models lying on or near the 1:1 line. Forcing from the subtropical Pacific generally makes a much smaller contribution, with the exception of a few models (Fig. 8b), which suggests that the forcing associated with advection of the mean vorticity by the anomalous divergent wind has a minor role in determining the extratropical response in our experiments. However, including this subtropical forcing does generally slightly improve the overall simulation of the North Pacific anomalous cyclonic circulation, so the remaining experiments presented in this section use forcing regions that extend between 30°N and 30°S.

We now examine the impact of varying the forcing (F') and basic state in turn to determine the role that changes in each have on the overall upper-level wind changes over the North Pacific. The use of two different F' and basic states means that four pairs of experiments can be performed. In each of these pairs, either F' or the basic state is varied from piControl to abrupt-4×CO_2, and the difference in NPAC meridional wind between each pair of experiments is shown in Fig. 9

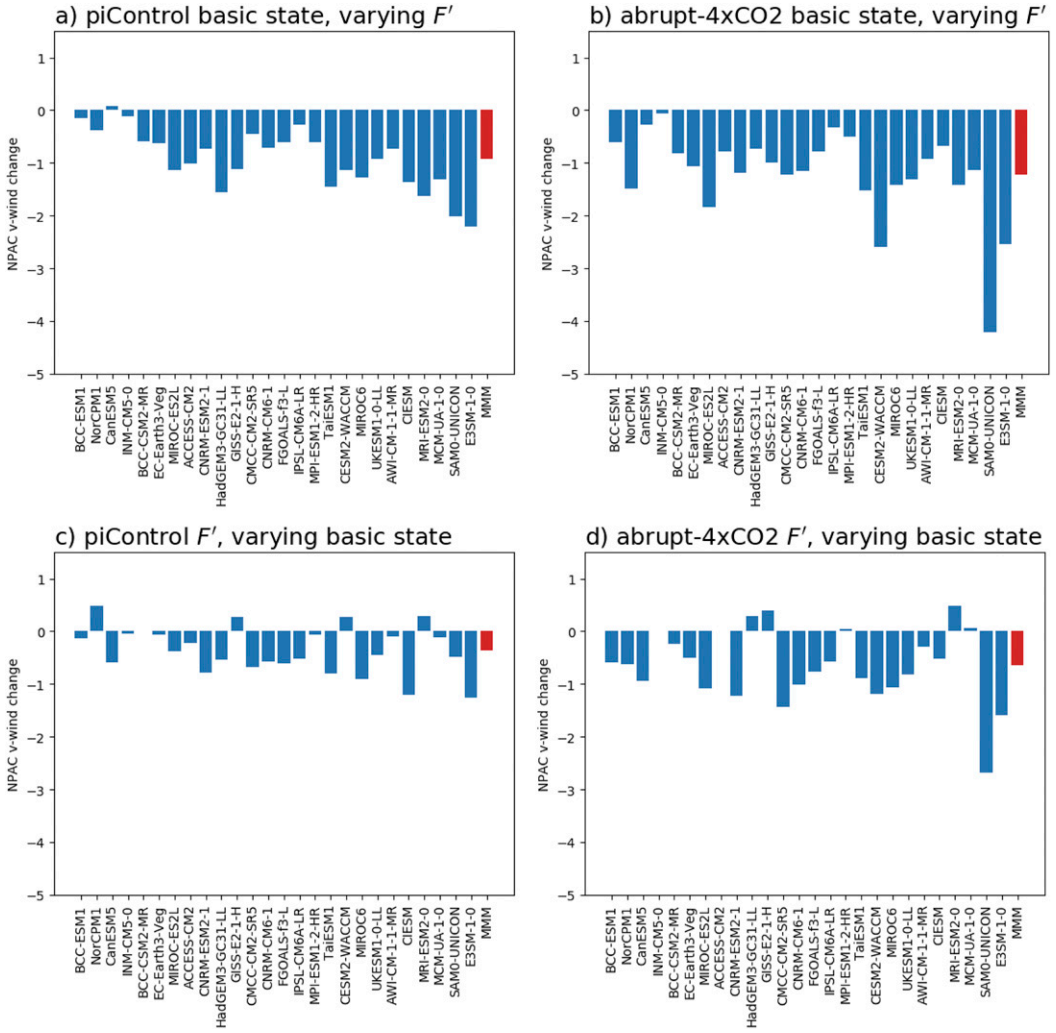

FIG. 9. Meridional wind anomaly change averaged over the NPAC region from barotropic model experiments run using (a) the piControl basic state, varying F', (b) the abrupt-4×CO_2 basic state, varying F', (c) the piControl F', varying the basic state, and (d) the abrupt-4×CO_2 F', varying the basic state. Changes to the forcing (F') make the largest contribution to the overall wind changes over the North Pacific, with negative changes for all but one model. Varying the basic state results in a much more inconsistent response, with more models with a positive wind change and a multimodel average that is around half that when varying F'.

(abrupt-4×CO_2 minus piControl). The upper two panels in this figure show the impact of varying F' from piControl to abrupt-4×CO_2 but keeping the same basic state, and the lower two panels show the impact of varying the basic state, but keeping the same F'. In all cases, F' is applied in the full tropical Pacific region used previously (30°N–30°S, 100°E–120°W).

By comparing the panels in Fig. 9 with Fig. 7b it can be seen that changes to F' (top two panels) make the largest contribution to the overall wind changes. In these experiments, the wind changes are negative for all but one model, and the average across all models is around $-1\,\mathrm{m\,s^{-1}}$ for both piControl and abrupt-4×CO_2 basic state. There is a small amount of nonlinearity as the response to F' does depend somewhat on the basic state used, although this does not change the overall conclusion. When varying the basic state but keeping the same F' (lower two panels) the response is more varied, with more models with a positive wind change and anomalies that are closer to zero overall, and an average across all models of around $-0.5\,\mathrm{m\,s^{-1}}$ or less. This suggests that it is changes to F' between piControl and abrupt-4×CO_2 that are the dominant driver of the circulation changes over the North Pacific and North America, rather than changes to the basic state.

We now divide the tropical Pacific forcing region into two separate longitudinal regions to determine where the most important changes to F' are occurring. For these experiments, we look at the NPAC meridional wind changes when varying both F' and the basic state. The first of these smaller forcing regions is centered over the Maritime Continent (30°N–30°S, 100°–150°E). This is in a similar location to the tropical west Pacific Rossby wave "hotspot" identified in Scaife et al. (2017)

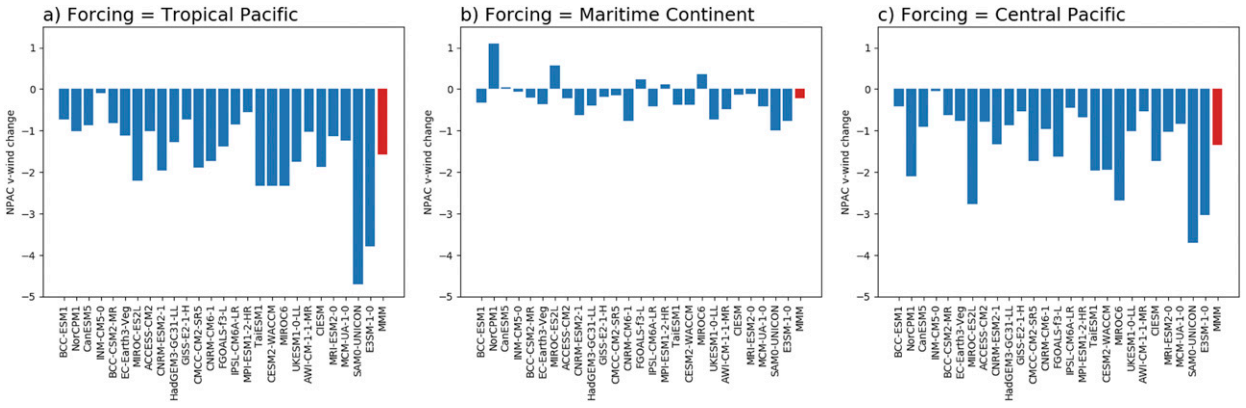

FIG. 10. Meridional wind anomaly change averaged over the NPAC region from barotropic model experiments varying both basic state and F', using (a) the full tropical Pacific forcing region, (b) forcing in the Maritime Continent, and (c) forcing in the central Pacific. Forcing in the central Pacific results in a much larger response than when forcing in the Maritime Continent, with wind changes that are similar in magnitude to those when using the full tropical Pacific forcing region. This suggests that changes to F' in the central Pacific are the main driver of circulation changes over the North Pacific.

as being an important source of extratropical Rossby waves in the Northern Hemisphere winter. Compared to the meridional wind changes in the full tropical Pacific forcing experiments (Fig. 10a) the wind changes when forcing only in the Maritime Continent are significantly smaller (Fig. 10b). The majority of models have a wind change that is very small, and the multimodel average is close to zero ($-0.22\,\mathrm{m\,s^{-1}}$).

The second of the smaller forcing regions is over the central Pacific (30°N–30°S, 150°E–120°W). This is in the region in which El Niño precipitation is projected to shift eastward under global warming. It is immediately obvious that the changes in this set of experiments (Fig. 10c) are of much larger magnitude than when forcing in the Maritime Continent, with a multimodel mean of $-1.35\,\mathrm{m\,s^{-1}}$, which is similar to that when using the full tropical Pacific forcing region (MMM of $-1.57\,\mathrm{m\,s^{-1}}$). This strongly suggests that changes to F' in the central Pacific, rather than the Maritime Continent/west Pacific, are the main driver of the circulation changes over the North Pacific and North America. This is in agreement with the results of Trenberth et al. (2014), who found that the central Pacific is the dominant source of extratropical wave activity, rather than the west Pacific.

As well as being projected to shift eastward under global warming, the magnitude of El Niño precipitation anomalies is also expected to change, with most models simulating an increase in abrupt-4×CO_2 compared to piControl (Fig. 3). This change in precipitation causes changes to the forcing field (F') due to changes in the upper-level divergence in the deep tropics. Changes to the interaction of the divergent wind with the jet stream in the subtropics also make a contribution, but this is small for most models (Fig. 8). When using F' from abrupt-4×CO_2 in the earlier experiments, this field contains changes due to both the longitude shift of precipitation and also changes associated with magnitude differences. Therefore, having established that changes to F' in the central Pacific are the most important in determining changes to the North America teleconnection, we now examine whether this is due to changes to the amplitude or as a result of the longitude shift of the forcing (or a combination of both).

To determine the contribution of changes to the amplitude of F', we run further barotropic model experiments, but instead of varying F' between piControl and abrupt-4×CO_2 we scale the piControl forcing field based on the projected changes to El Niño precipitation. F' is scaled by the same amount at all points within the forcing region, but using a different scaling factor for each of the CMIP6 models. This value is based on the change to the maximum precipitation anomaly within a central equatorial Pacific region (abrupt-4×CO_2 divided by piControl precipitation maxima) and the scaling factors used for the different CMIP6 models can be found in Table 1.

To examine the role of the longitudinal shift of F', the piControl forcing field within the central Pacific region is shifted either east or west. This shift is based on the location of the maximum change in precipitation between piControl and abrupt-4×CO_2 relative to the longitude of the piControl precipitation maximum, and the longitude shifts used are shown in Table 1. In agreement with previous studies (e.g., Knutson and Manabe 1995; Meehl and Washington 1996; Boer et al. 2004) all but two models have an overall eastward shift using this metric. As with the amplified experiments, the whole F' field is shifted by the same amount, but is still applied within the central Pacific region used previously. Both the scaled and shifted forcings are applied to the piControl basic state and differences for both are computed relative to the experiments run using the original piControl basic state and F'.

The changes for the amplified F' are shown in Fig. 11a, and for the shifted F' are in Fig. 11b. The changes in the amplified experiments are generally small, with all differences between -1 and $1\,\mathrm{m\,s^{-1}}$ and a small, positive multimodel average. However, the longitudinally shifted forcings result in much larger differences overall, which are of similar magnitude to those in Fig. 10c and almost all of which are negative. This suggests that the overall eastward shift of precipitation anomalies dominates over the changes to the magnitude of precipitation anomalies, which,

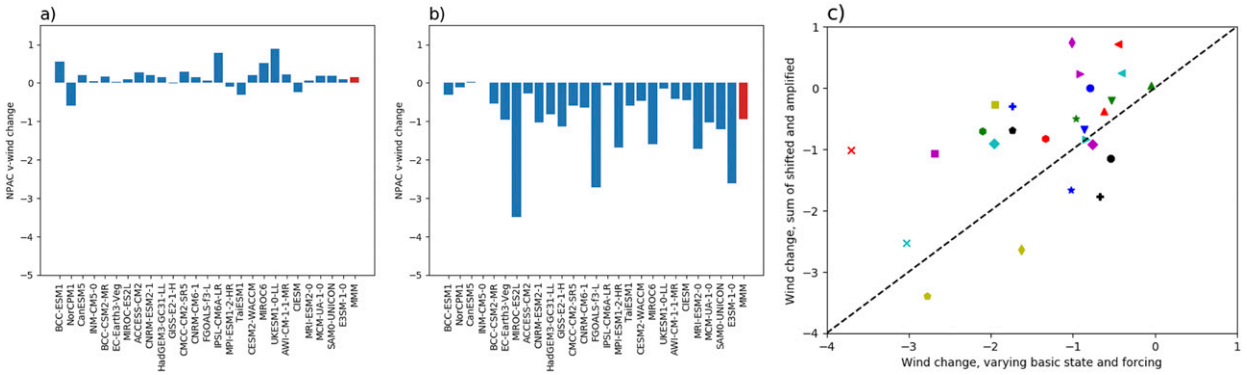

FIG. 11. Meridional wind anomaly change averaged over the NPAC region from barotropic model experiments forced in the central Pacific region using (a) F' from piControl scaled according to the simulated change in magnitude of El Niño precipitation between piControl and abrupt-4×CO_2 and (b) piControl F' shifted longitudinally based on the simulated change in longitude of El Niño precipitation. Wind changes in both experiments are relative to the experiment run using the original piControl basic state and F'. (c) The sum of the wind changes from the scaled and longitudinally shifted experiments vs the wind change when using the original full varying F'. The symbols used for each CMIP6 model can be found in the appendix. Shifting F' longitudinally results in a much larger negative NPAC wind difference than when using the scaled F'. This suggests that the overall eastward shift of El Niño precipitation in the central Pacific is the dominant driver of the circulation changes over the North Pacific.

in the absence of other changes, might be expected to result in a slight strengthening of circulation anomalies over North America. When taking the sum of the differences from the scaled and shifted experiments, and comparing these to the differences in the full central Pacific forcing experiments (run using the original piControl and abrupt-4×CO_2 F') there is a reasonably strong correlation (0.52) and the experiments run using different models tend to sit near the 1:1 line (Fig. 11c). This suggests that, despite the simplicity of the method used to determine the forcing shift and scaling, and the linear manner in which it was applied to the F' fields, that the contribution of each of these changes to the overall change in F' in abrupt-4×CO_2 is quite accurately represented in these experiments.

Therefore, the simulated overall eastward shift of El Niño precipitation in the central Pacific appears to be the dominant driver of circulation changes over the North Pacific region, rather than changes to the strength of precipitation anomalies or changes in the basic state, and is therefore likely to be the main cause of the projected weakening of El Niño surface temperature anomalies over North America seen in the abrupt-4×CO_2 simulations.

4. Summary and conclusions

Changes to the El Niño temperature teleconnection to North America in the CMIP6 abrupt-4×CO_2 simulations relative to the preindustrial control (piControl) are analyzed for 26 models. In piControl all 26 models simulate El Niño temperature and circulation anomalies that are qualitatively similar to those from the ERA5 reanalysis. El Niño events in both are associated with an anomalously deep Aleutian low, which drives the advection of warmer air northward, resulting in positive temperature anomalies over Alaska and much of northern North America.

In the abrupt-4×CO_2 simulations the positive temperature anomalies over northern North America are weakened or have the opposite sign in 22 out of 26 models, with 15 of these statistically significant at the 5% level. Meehl and Teng (2007) found that changes to the North America teleconnection are stronger and more consistent in models with an increase in El Niño amplitude, but we find that changes are consistent across models with both an increase and a decrease in the amplitude of the Niño-3.4 index in abrupt-4×CO_2 compared to piControl. This change in North America temperature anomaly is closely related to changes to the circulation anomalies over the North Pacific at both upper and lower levels, associated with changes in both the position and strength of the anomalous Aleutian low.

A linear barotropic model forced by the tropical Pacific Rossby wave source (RWS), which is associated with El Niño precipitation, is able to broadly capture the El Niño anomalous cyclonic circulation over the North Pacific, as well as a reasonable amount of the CMIP6 ensemble variability. This suggests that linearity in the relative influence of changes to the basic state and anomalous forcing to the overall changes in the El Niño–North America teleconnection is a good approximation. By running this model with the basic state and forcing (RWS) from the piControl and abrupt-4×CO_2 simulations of the individual CMIP6 models, it is found that changes to the forcing in the equatorial Pacific are the main cause of the circulation changes over the North Pacific, rather than changes in the basic state. Previous studies have disagreed on the relative roles of changes to El Niño properties and the extratropical mean background state in the overall North America teleconnection changes. Some, such as Meehl et al. (2006) and Meehl and Teng (2007), argue that a decrease in the upper-level streamfunction near the west coast of North America in association with increased greenhouse gas concentrations, which is independent of ENSO, makes an important contribution to the eastward shift of the North America teleconnection pattern. Müller and Roeckner (2008) also suggest that changes to

the mean state have an influence on the teleconnection changes. Others, however, such as Kug et al. (2010) find that changes in the equatorial Pacific relating to ENSO properties are most important. Our results suggest that it is changes to the equatorial Pacific RWS forcing, associated with changes to El Niño, that have the largest influence on teleconnection changes, and although there are slight contributions from basic state changes, these are much smaller and more inconsistent. All the aforementioned studies used either single models or small ensembles, which may go some way to explaining the different results. Here, we have used a large ensemble of climate models, and the largely consistent response seen suggests that our results are robust.

The most important of the changes to the RWS forcing occur in the central Pacific, rather than the Maritime Continent, with North Pacific wind changes when forcing in the central Pacific similar to those when using the whole tropical Pacific forcing region, and much smaller changes when only forcing in the Maritime Continent. In the central Pacific, it is the overall eastward shift of El Niño precipitation in this region, rather than changes to its magnitude, that is the most important factor in driving the circulation changes over the North Pacific. This eastward shift of precipitation results in an eastward shift of the associated anomalous cyclonic circulation. This means that air that is advected northward is of relatively cool continental origin, rather than warmer oceanic air, and so is less anomalously warm when it reaches northern North America; hence there is an overall reduction in North America El Niño temperature anomalies.

Despite the robustness of the projected change to the background equatorial Pacific SST gradient and subsequent eastward shift of El Niño precipitation that is seen in the CMIP6 ensemble, such a change has yet to be observed in association with the rising greenhouse gas concentrations seen over the last century (Seager et al. 2019). Therefore, the results presented here further demonstrate that it is vitally important that the reasons for this discrepancy are understood, to enable more accurate future projections of North American climate to be made.

Acknowledgments. This work was funded by the Natural Environment Research Council (NERC) through the Emergence of Climate Hazards project (NE/S004645/1). We also thank the three anonymous reviewers for their constructive comments that helped to improve the manuscript.

Data availability statement. The CMIP6 data used in this study are available for download at https://esgf-node.llnl.gov/search/cmip6/. ERA5 data are available for download from the Copernicus Climate Change Service Climate Data Store at https://cds.climate.copernicus.eu/#!/search?text=ERA5&type=dataset.

APPENDIX

Scatter Plot Symbols

Scatter plot symbols are shown in Fig. A1.

Model	Scatter symbol
ACCESS-CM2	●
AWI-CM-1-1-MR	▼
BCC-CSM2-MR	▲
BCC-ESM1	◀
CanESM5	▶
CESM2-WACCM	■
CIESM	⬟
CMCC-CM2-SR5	✚
CNRM-CM6-1	★
CNRM-ESM2-1	●
E3SM-1-0	×
EC-Earth3-Veg	◆
FGOALS-f3-L	◆
GISS-E2-1-H	●
HadGEM3-GC31-LL	▼
INM-CM5-0	▲
IPSL-CM6A-LR	◀
MCM-UA-1-0	▶
MIROC6	■
MIROC-ES2L	⬟
MPI-ESM1-2-HR	✚
MRI-ESM2-0	★
NorCPM1	●
SAM0-UNICON	×
TaiESM1	◆
UKESM1-0-LL	◆

FIG. A1. Symbols used in scatterplots to represent each CMIP6 model.

REFERENCES

Ambrizzi, T., B. J. Hoskins, and H.-H. Hsu, 1995: Rossby wave propagation and teleconnection patterns in the austral winter. *J. Atmos. Sci.*, **52**, 3661–3672, https://doi.org/10.1175/1520-0469(1995)052<3661:RWPATP>2.0.CO;2.

Boer, G., B. Yu, S.-J. Kim, and G. Flato, 2004: Is there observational support for an El Niño-like pattern of future global warming? *Geophys. Res. Lett.*, **31**, L06201, https://doi.org/10.1029/2003GL018722.

Brown, J. R., and Coauthors, 2020: Comparison of past and future simulations of ENSO in CMIP5/PMIP3 and CMIP6/PMIP4 models. *Climate Past*, **16**, 1777–1805, https://doi.org/10.5194/cp-16-1777-2020.

Cai, W., and Coauthors, 2014: Increasing frequency of extreme El Niño events due to greenhouse warming. *Nat. Climate Change*, **4**, 111–116, https://doi.org/10.1038/nclimate2100.

——, and Coauthors, 2018: Increased variability of eastern Pacific El Niño under greenhouse warming. *Nature*, **564**, 201–206, https://doi.org/10.1038/s41586-018-0776-9.

Christensen, J. H., and Coauthors, 2013: Climate phenomena and their relevance for future regional climate change. *Climate Change 2013: The Physical Science Basis*, T. F. Stocker et al., Eds., Cambridge University Press, 1217–1308.

Collins, M., and Coauthors, 2010: The impact of global warming on the tropical Pacific Ocean and El Niño. *Nat. Geosci.*, **3**, 391–397, https://doi.org/10.1038/ngeo868.

Deser, C., I. R. Simpson, A. S. Phillips, and K. A. McKinnon, 2018: How well do we know ENSO's climate impacts over North America, and how do we evaluate models accordingly? *J. Climate*, **31**, 4991–5014, https://doi.org/10.1175/JCLI-D-17-0783.1.

Eyring, V., S. Bony, G. A. Meehl, C. A. Senior, B. Stevens, R. J. Stouffer, and K. E. Taylor, 2016: Overview of the Coupled Model Intercomparison Project phase 6 (CMIP6) experimental design and organization. *Geosci. Model Dev.*, **9**, 1937–1958, https://doi.org/10.5194/gmd-9-1937-2016.

Fredriksen, H.-B., J. Berner, A. C. Subramanian, and A. Capotondi, 2020: How does El Niño–Southern Oscillation change under global warming—A first look at CMIP6. *Geophys. Res. Lett.*, **47**, e2020GL090640, https://doi.org/10.1029/2020GL090640.

Grimm, A. M., and P. L. Silva Dias, 1995: Use of barotropic models in the study of the extratropical response to tropical heat sources. *J. Meteor. Soc. Japan*, **73**, 765–780, https://doi.org/10.2151/jmsj1965.73.4_765.

Guilyardi, E., H. Bellenger, M. Collins, S. Ferrett, W. Cai, and A. Wittenberg, 2012: A first look at ENSO in CMIP5. *CLIVAR Exchanges*, No. 17, International CLIVAR Project Office, Southampton, United Kingdom, 29–32.

Hersbach, H., and Coauthors, 2020: The ERA5 global reanalysis. *Quart. J. Roy. Meteor. Soc.*, **146**, 1999–2049, https://doi.org/10.1002/qj.3803.

Hoerling, M. P., A. Kumar, and M. Zhong, 1997: El Niño, La Niña, and the nonlinearity of their teleconnections. *J. Climate*, **10**, 1769–1786, https://doi.org/10.1175/1520-0442(1997)010<1769:ENOLNA>2.0.CO;2.

Holland, M. M., and C. M. Bitz, 2003: Polar amplification of climate change in coupled models. *Climate Dyn.*, **21**, 221–232, https://doi.org/10.1007/s00382-003-0332-6.

Horel, J. D., and J. M. Wallace, 1981: Planetary-scale atmospheric phenomena associated with the southern oscillation. *Mon. Wea. Rev.*, **109**, 813–829, https://doi.org/10.1175/1520-0493(1981)109<0813:PSAPAW>2.0.CO;2.

Hoskins, B. J., and T. Ambrizzi, 1993: Rossby wave propagation on a realistic longitudinally varying flow. *J. Atmos. Sci.*, **50**, 1661–1671, https://doi.org/10.1175/1520-0469(1993)050<1661:RWPOAR>2.0.CO;2.

Knutson, T. R., and S. Manabe, 1995: Time-mean response over the tropical Pacific to increased CO_2 in a coupled ocean–atmosphere model. *J. Climate*, **8**, 2181–2199, https://doi.org/10.1175/1520-0442(1995)008<2181:TMROTT>2.0.CO;2.

Kug, J.-S., S.-I. An, Y.-G. Ham, and I.-S. Kang, 2010: Changes in El Niño and La Niña teleconnections over North Pacific–America in the global warming simulations. *Theor. Appl. Climatol.*, **100**, 275–282, https://doi.org/10.1007/s00704-009-0183-0.

McKinnon, K. A., and C. Deser, 2018: Internal variability and regional climate trends in an observational large ensemble. *J. Climate*, **31**, 6783–6802, https://doi.org/10.1175/JCLI-D-17-0901.1.

Meehl, G. A., and W. M. Washington, 1996: El Niño-like climate change in a model with increased atmospheric CO2 concentrations. *Nature*, **382**, 56–60, https://doi.org/10.1038/382056a0.

——, and H. Teng, 2007: Multi-model changes in El Niño teleconnections over North America in a future warmer climate. *Climate Dyn.*, **29**, 779–790, https://doi.org/10.1007/s00382-007-0268-3.

——, ——, and G. Branstator, 2006: Future changes of El Niño in two global coupled climate models. *Climate Dyn.*, **26**, 549–566, https://doi.org/10.1007/s00382-005-0098-0.

Michel, C., C. Li, I. R. Simpson, I. Bethke, M. P. King, and S. Sobolowski, 2020: The change in the ENSO teleconnection under a low global warming scenario and the uncertainty due to internal variability. *J. Climate*, **33**, 4871–4889, https://doi.org/10.1175/JCLI-D-19-0730.1.

Müller, W., and E. Roeckner, 2008: ENSO teleconnections in projections of future climate in ECHAM5/MPI-OM. *Climate Dyn.*, **31**, 533–549, https://doi.org/10.1007/s00382-007-0357-3.

O'Reilly, C. H., T. Woollings, L. Zanna, and A. Weisheimer, 2018: The impact of tropical precipitation on summertime Euro-Atlantic circulation via a circumglobal wave train. *J. Climate*, **31**, 6481–6504, https://doi.org/10.1175/JCLI-D-17-0451.1.

Power, S., F. Delage, C. Chung, G. Kociuba, and K. Keay, 2013: Robust twenty-first-century projections of El Niño and related precipitation variability. *Nature*, **502**, 541–545, https://doi.org/10.1038/nature12580.

Ropelewski, C. F., and M. S. Halpert, 1986: North American precipitation and temperature patterns associated with the El Niño/Southern Oscillation (ENSO). *Mon. Wea. Rev.*, **114**, 2352–2362, https://doi.org/10.1175/1520-0493(1986)114<2352:NAPATP>2.0.CO;2.

Sardeshmukh, P. D., and B. J. Hoskins, 1988: The generation of global rotational flow by steady idealized tropical divergence. *J. Atmos. Sci.*, **45**, 1228–1251, https://doi.org/10.1175/1520-0469(1988)045<1228:TGOGRF>2.0.CO;2.

Scaife, A. A., and Coauthors, 2017: Tropical rainfall, Rossby waves and regional winter climate predictions. *Quart. J. Roy. Meteor. Soc.*, **143**, 1–11, https://doi.org/10.1002/qj.2910.

Seager, R., M. Cane, N. Henderson, D.-E. Lee, R. Abernathey, and H. Zhang, 2019: Strengthening tropical Pacific zonal sea surface temperature gradient consistent with rising greenhouse gases. *Nat. Climate Change*, **9**, 517–522, https://doi.org/10.1038/s41558-019-0505-x.

Sterl, A., G. J. van Oldenborgh, W. Hazeleger, and G. Burgers, 2007: On the robustness of ENSO teleconnections. *Climate Dyn.*, **29**, 469–485, https://doi.org/10.1007/s00382-007-0251-z.

Stevenson, S., 2012: Significant changes to ENSO strength and impacts in the twenty-first century: Results from CMIP5. *Geophys. Res. Lett.*, **39**, L17703, https://doi.org/10.1029/2012GL052759.

——, B. Fox-Kemper, M. Jochum, R. Neale, C. Deser, and G. Meehl, 2012: Will there be a significant change to El Niño in the twenty-first century? *J. Climate*, **25**, 2129–2145, https://doi.org/10.1175/JCLI-D-11-00252.1.

Trenberth, K. E., 1997: The definition of El Niño. *Bull. Amer. Meteor. Soc.*, **78**, 2771–2778, https://doi.org/10.1175/1520-0477(1997)078<2771:TDOENO>2.0.CO;2.

——, J. T. Fasullo, G. Branstator, and A. S. Phillips, 2014: Seasonal aspects of the recent pause in surface warming. *Nat. Climate Change*, **4**, 911–916, https://doi.org/10.1038/nclimate2341.

van Oldenborgh, G. J., S. Y. Philip, and M. Collins, 2005: El Niño in a changing climate: A multi-model study. *Ocean Sci.*, **1**, 81–95, https://doi.org/10.5194/os-1-81-2005.

Wallace, J. M., and D. S. Gutzler, 1981: Teleconnections in the geopotential height field during the Northern Hemisphere winter. *Mon. Wea. Rev.*, **109**, 784–812, https://doi.org/10.1175/1520-0493(1981)109<0784:TITGHF>2.0.CO;2.

Xie, S.-P., C. Deser, G. A. Vecchi, J. Ma, H. Teng, and A. T. Wittenberg, 2010: Global warming pattern formation: Sea surface temperature and rainfall. *J. Climate*, **23**, 966–986, https://doi.org/10.1175/2009JCLI3329.1.

Yeh, S.-W., and Coauthors, 2018: ENSO atmospheric teleconnections and their response to greenhouse gas forcing. *Rev. Geophys.*, **56**, 185–206, https://doi.org/10.1002/2017RG000568.